nature communications

Article

https://doi.org/10.1038/s41467-025-57663-3

Understanding capacity fading from structural degradation in Prussian blue analogues for wide-temperature sodium-ion cylindrical battery

Received: 13 September 2024

Accepted: 27 February 2025

Published online: 13 March 2025

Check for updates

Hang Zhang[1,2], Jiayang Li[2], Jinhang Liu[3], Yun Gao[1] ✉, Yameng Fan[2], Xiaohao Liu[1], Chaofei Guo[4], Haoxuan Liu[2], Xiudong Chen[3] ✉, Xingqiao Wu[1], Yang Liu[4], Qinfen Gu[5], Li Li[4] ✉, Jiazhao Wang[1,2] & Shu-Lei Chou[1] ✉

Low-cost Fe-based Prussian blue analogues often suffer from capacity degradation, resulting in continuous energy loss, impeding commercialization for practical sodium-ion batteries. The underlying cause of capacity decrease remains mysterious. Herein, we show that irreversible phase transitions, structural degradation, deactivation of surface redox centres, and dissolution of transition metal ions in Prussian blue analogues accumulate continuously during cycling. These undesirable changes are responsible for massive destruction of their morphology, leading to the capacity decay. A dual regulation strategy is applied to alleviate the above-mentioned problems of Prussian blue analogues. The designed 18650/33140 cylindrical cells using modified Prussian blue analogues and hard carbon display improved cycling stability and wide-temperature working performance (−40 °C–100 °C). The findings resolve the controversy over the origins of Prussian blue analogues cathode degradation, emphasize the necessity of eliminating irreversible crystal/structural changes to guarantee enhanced cycling stability, and demonstrate the potential of Prussian blue analogues cathode for commercial sodium-ion batteries.

Energy storage systems (ESSs) with renewable energy sources designed for smart grids are expected to address the problems associated with energy shortages and the environment. Since sodium reserves are abundant and easily accessible, sodium-ion batteries (SIBs) exhibit promising potential for large-scale ESSs[1–3]. A stable, long-cycle system is associated with reduced operating and maintenance costs, which is one of the most important aspects of large-scale ESSs[4–6]. Therefore, SIBs possess the key competitive features of being inexpensive and stable because they use long-cycling stable electrodes that contain only cheap elements. Several cathode materials have been extensively explored for SIBs in recent years, including layered oxides, polyanionic compounds, and Prussian blue analogues (PBAs)[7–10]. P2-type $A_2Ni_2TeO_6$ (A = Na, K), with large layer spacing which facilitates reversible intercalation, exhibits good cycling stability and ionic

[1]Institute for Carbon Neutralization Technology, College of Chemistry and Materials Engineering, Wenzhou University, Wenzhou, Zhejiang, PR China. [2]Institute for Superconducting and Electronic Materials, Australian Institute for Innovative Materials, University of Wollongong, Innovation Campus, Squires Way, North Wollongong, NSW, Australia. [3]School of Chemistry and Chemical Engineering, Jiangxi Province Engineering Research Center of Ecological Chemical Industry, Jiujiang University, Jiujiang, China. [4]School of Environmental and Chemical Engineering, Shanghai University, Shanghai, PR China. [5]Australian Synchrotron (ANSTO) 800 Blackburn Road, Clayton, VIC, Australia. ✉e-mail: YunGao1995@shu.edu.cn; chenxd@jju.edu.cn; LILI2020@shu.edu.cn; chou@wzu.edu.cn

diffusion capability for SIBs[11,12]. Meanwhile, PBAs are highly promising for practical applications due to their high theoretical specific energy, low cost, and ease of large-scale preparation[13–15]. $AT1[T2(CN)_6]_y\square_{1-y}\cdot zH_2O$ is an appropriate chemical formula to represent PBAs. In this case, A represents an alkali metal, T1 and T2 are transition metals joined by C≡N bonds, and □ represents the defects caused by the loss of $T2(CN)_6$ groups. PBAs are highly promising cathode materials for SIBs due to their high theoretical capacity (up to 170 mAh g^{-1}), three-dimensional open framework, and cost-effectiveness. Additionally, PBAs are inexpensive and easy to synthesize via scalable methods such as co-precipitation. These advantages have enabled the development of PBA-based batteries for applications like automotive start-stop systems, two-wheeled vehicles, and sightseeing boats. Future applications, such as grid energy storage systems (ESS), also hold significant promise, as PBAs can compete with lithium iron phosphate batteries in terms of cost and scalability, potentially capturing up to 50% of their market share.

Challenges remain in fully realizing the industrialization potential of PBAs, such the universal capacity decreases over long periods of time, however[15,16]. Crystalline water removal is a critical issue, as its presence leads to gas generation during cycling, while complete removal can distort the lattice and affect stability. PBAs also suffer from low electronic conductivity, necessitating additional modifications such as carbon coating or doping, which can increase complexity and cost. Investigations to deepen our basic understanding and improve the material development of PBAs have been conducted to improve their cycling stability[14,17–19]. Until recently, their capacity degradation has been primarily attributed to $Fe(CN)_6^{4-}$ vacancies and highly coordinated/crystal water content in the initial structure, while the effects of structural deformation and the loss of active redox centres induced during cycling were not adequately recognized. As a result of the parasitism of coordinated/crystal water, Na^+ storage in the PBA framework is insufficient, and the diffusion of Na^+ is slowed[16,17]. The framework of PBAs is vulnerable to collapse due to excessive randomly distributed $[Fe(CN)_6]^{4-}$ vacancies. Several previous studies have also been conducted to improve their cycling stability, including crystal structure optimization, surface coating, removal of water, and element substitution[16,18,20–22]. Despite these strategies, the stability of their cycling performance still needs improvement due to unclear capacity fade mechanism.

One of the most prevalent reasons for the capacity decrease in PBAs is their irreversible phase transition. Several studies have shown that PBAs undergo a two- or three-step phase change when cycling (e.g., rhombohedral ↔ cubic ↔ tetragonal)[23–25]. As sodium ions move into and out of the PBA framework, they will cause a dynamic structural evolution that has a direct impact on its structural stability and electrochemical properties. These electrodes frequently exhibit unbalanced intercalation and deintercalation of sodium ions, resulting in unstable structural behavior on the macroscopic and microscopic levels[26,27]. There are two categories of mechanical degradation: volume change and mechanical strain, which are widely recognized as the underlying causes of mechanical damage, such as cracks and breaks[28–30]. In addition, nanoscale tensions result in less noticeable lattice changes, which are detrimental to the durability of existing structures[31,32]. Because they are inextricably coupled with one another during electrochemical processes, it is difficult to determine the precise role of these structural degradations and where they originated. Undoubtedly, establishing the mechanistic connection between nanoscale framework behavior and electrochemical characteristics requires comprehensive studies comprising numerous length scales, which are likely to have the benefit of unveiling the preceding capacity decline of PBAs and pointing out efficient strategies for minimizing capacity loss[33,34].

Here, we reveal the mechanism for the capacity decrease of PBAs on the macroscopic and microscopic levels by comparing three PBA materials with different crystal structures, defects, and water content. During cycling, irreversible phase transitions and structural degradation are the principal factors responsible for capacity decreases in PBA cathodes. It is discovered that high lattice distortion plays a significant role in triggering destructive structural degradation in PBA cathodes, resulting in significant structural breakdown and fragmentation during a long cycling process. The loss of electrochemically active centres on the electrode surface and the dissolution of transition metal ions, which accumulates continuously during cycling, are also confirmed. According to the above-mentioned problems, a dual regulation strategy (coordination environment and crystal nucleation growth) is applied for improving the stability of PBAs during the cycling process. In addition, the designed 18650/33140 cylindrical cells using modified PBAs and hard carbon display enhanced cycling stability (80% capacity/energy retention after 1000 cycles) and wide temperature working ability (−40 °C–100 °C). We believe that this work helps towards addressing the dispute related to the origins of PBA cathodes' capacity decrease and demonstrates the potential of PBA cathode for large-scale commercialization toward practical SIBs with long cycle life and wide temperature range.

Results

Materials characterizations

The type and amount of host elements in the PBA crystal structure can be changed by using different precursors during synthesis. So, three PBAs with high sodium content, medium sodium content, and sodium free, were synthesized through the co-precipitation method and are denoted as HSPB, MSPB, and LSPB. Powder X-ray diffraction (XRD) of the as-synthesized PBAs was analysed by Rietveld refinement using GSAS software[35]. Detailed descriptions of the crystal structure are provided in Supplementary Table 1–3 in the Supporting Information. As shown in Fig. 1a, HSPB exhibits rhombohedral phase (lattice parameters: $a = 7.4832$ Å, $c = 17.5592$ Å, $V = 851.54$ Å^3) with distinct sharp peaks, indicating good crystallinity and a lower amount of $[Fe(CN)_6]^{4-}$ defects in the framework. The diffraction peaks of the (220) planes around 24° are split because of the decreased symmetry caused by the increased number of Na^+ per formula unit[25]. When there is less or no sodium in the framework, MSPB ($a = 10.2676$ Å, $V = 1082.44$ Å^3) and LSPB ($a = 10.22648$ Å, $V = 1069.49$ Å^3) have the cubic phase (Fm-3m) with no impurities (Fig. 1b, c). The broader peaks of the MSPB compared to the HSPB or LSPB mean smaller crystallite sizes. Scanning electron microscope (SEM) images and elemental mapping images for the three PBA samples are shown in Supplementary Figs. 1–5. As a chelating agent and sodium supplement, sodium citrate played a crucial part in the crystallization process, which was beneficial for slowing the rate of precipitation and raising the amount of sodium in the PBAs[14,17]. After adding the chelating agent, single microcubes (3–5 μm) were obtained in the HSPB. It was easier for MSPB to aggregate into larger secondary particles because of its nanosized primary particles (Supplementary Fig. 4). The elemental mapping images and X-ray photoelectron spectroscopy (XPS) spectra of LSPB provided in the Supplementary Fig. 5 prove that there was no potassium and sodium element in the LSPB. As illustrated in Fig. 1d–f, in-situ heating XRD characterization (flowing high purity Ar atmosphere) was performed to explore the thermal durability and how the structure changed during the dehydration of the three PBAs (25–400 °C). The different phase transition processes observed in the initial products are primarily influenced by their sodium content and crystal defects. The XRD data for the three PBAs exhibited no change below 150 °C. When the temperature was raised above 150 °C, the XRD pattern of HSPB (highest sodium content with a rhombohedral phase) changed significantly. From this temperature on, the peak positions of HSPB shifted to higher degrees, and new peaks were generated, which could be indexed as a new trigonal structure without water. A similar change was also found in MSPB (enhanced structural stability by more sodium

https://doi.org/10.1038/s41467-025-57663-3

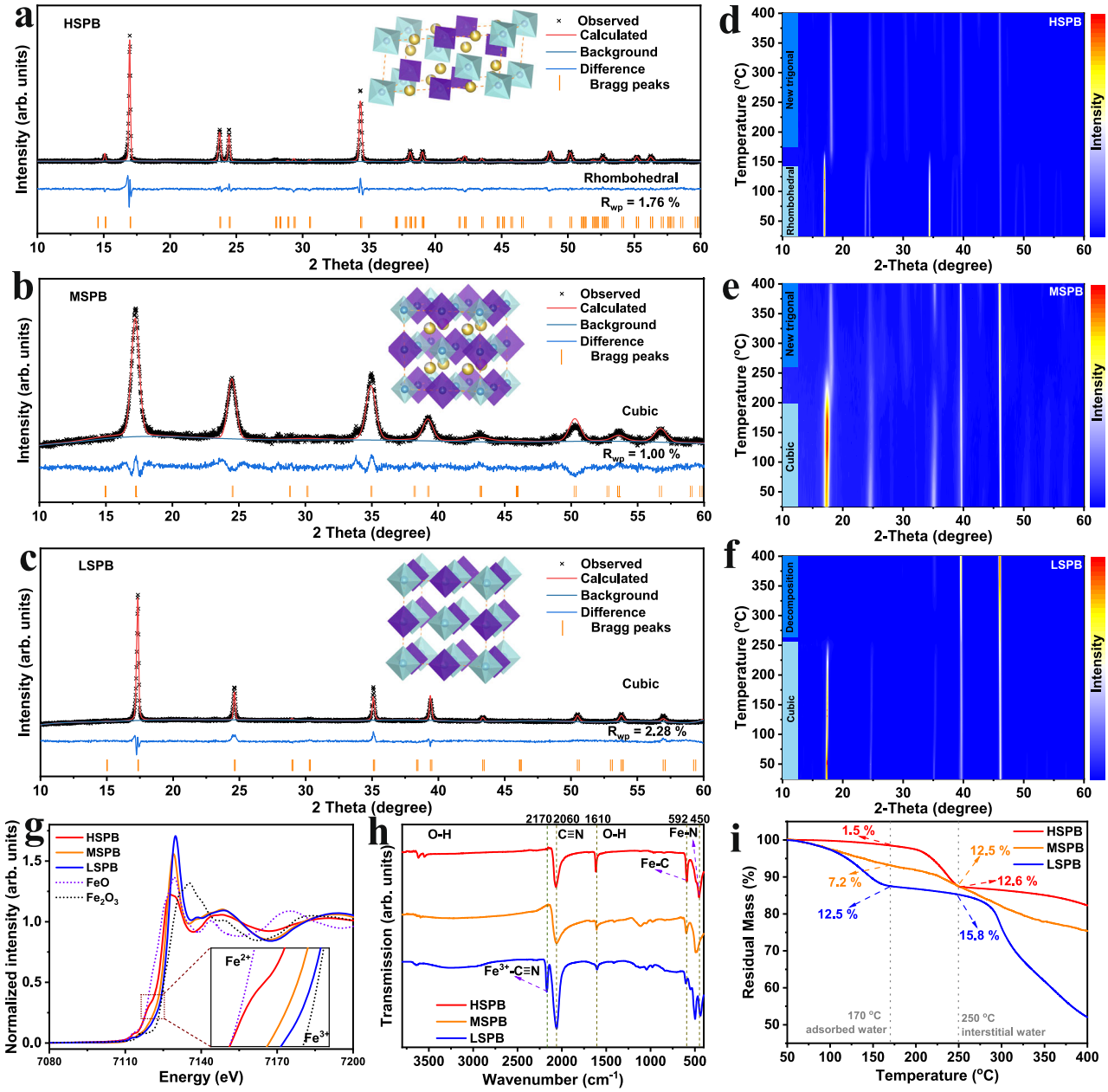

Fig. 1 | Structural characterizations. a–c Rietveld refinements of HSPB, MSPB, and LSPB. The golden spheres represent sodium ions, and the purple and green octahedrons represent low-spin and high-spin iron. **d–f** In-situ heating XRD of HSPB, MSPB, and LSPB. **g** Fe K-edge XANES spectra. **h** FTIR spectra. **i** TGA curves. The displayed percentages within panel are mass loss.

and fewer defects), but MSPB was stable up to 200 °C, and then the phase transition occurred. If the temperature exceeded 250 °C, the crystal structure of LSPB started to collapse due to thermal decomposition because of the reduced structural stability. This means that PBAs with more sodium content have a lower phase transition temperature when heated but can maintain the crystal structure up to 400 °C. The PBAs without sodium ions in the framework will decompose rapidly after a certain temperature (such as 250 °C for LSPB).

X-ray absorption spectroscopy (XAS) was performed on the Fe K-edge to investigate changes in the local electrical and structural properties in the three PBAs. As shown in the X-ray absorption near-edge structure (XANES) spectrum in Fig. 1g, the Fe K-edge absorption rising edges move slightly towards lower energy when there are more Na ions in the framework, suggesting that the Fe valence state of HSPB is mainly 2+, while that of LSPB is mainly 3+[36]. The Fourier-transformed intensities of the Fe K-edge extended X-ray absorption fine structure (EXAFS) spectra of the three PBAs are provided in Supplementary Fig. 6. The two peaks at 2094 and 2127 cm^{-1} of HSPB are the vibrations of Fe^{2+}-C≡N-Fe^{2+} and Fe^{2+}-C≡N-$Fe^{(3-x)+}$, which means that some ferrous ions were oxidized during synthesis (Supplementary Fig. 7). Only a peak at 2151 cm^{-1} (Fe^{3+}-C≡N-Fe^{3+}) was found in LSPB, indicating that only Fe^{3+} ions were linked with the cyano groups[37]. Fourier transform infrared (FTIR) spectroscopy was also performed, and the corresponding spectra of the PBAs are displayed in Fig. 1h. The strong peaks at 2160 and 2170 cm^{-1} correspond to the stretching vibrations of the C≡N bonds[34]. Moreover, the peaks at 1610 and around 3610 cm^{-1} represent the bending vibration of O-H and the corresponding O-H bond stretching, indicating the presence of H_2O[18]. Therefore, thermogravimetric analysis (TGA) was used to determine the water content of the PBAs (Fig. 1i). The water content of the PBAs was categorized into three categories: adsorbed water, interstitial water, and coordinated water. Water adsorbed on the surface was removed

https://doi.org/10.1038/s41467-025-57663-3

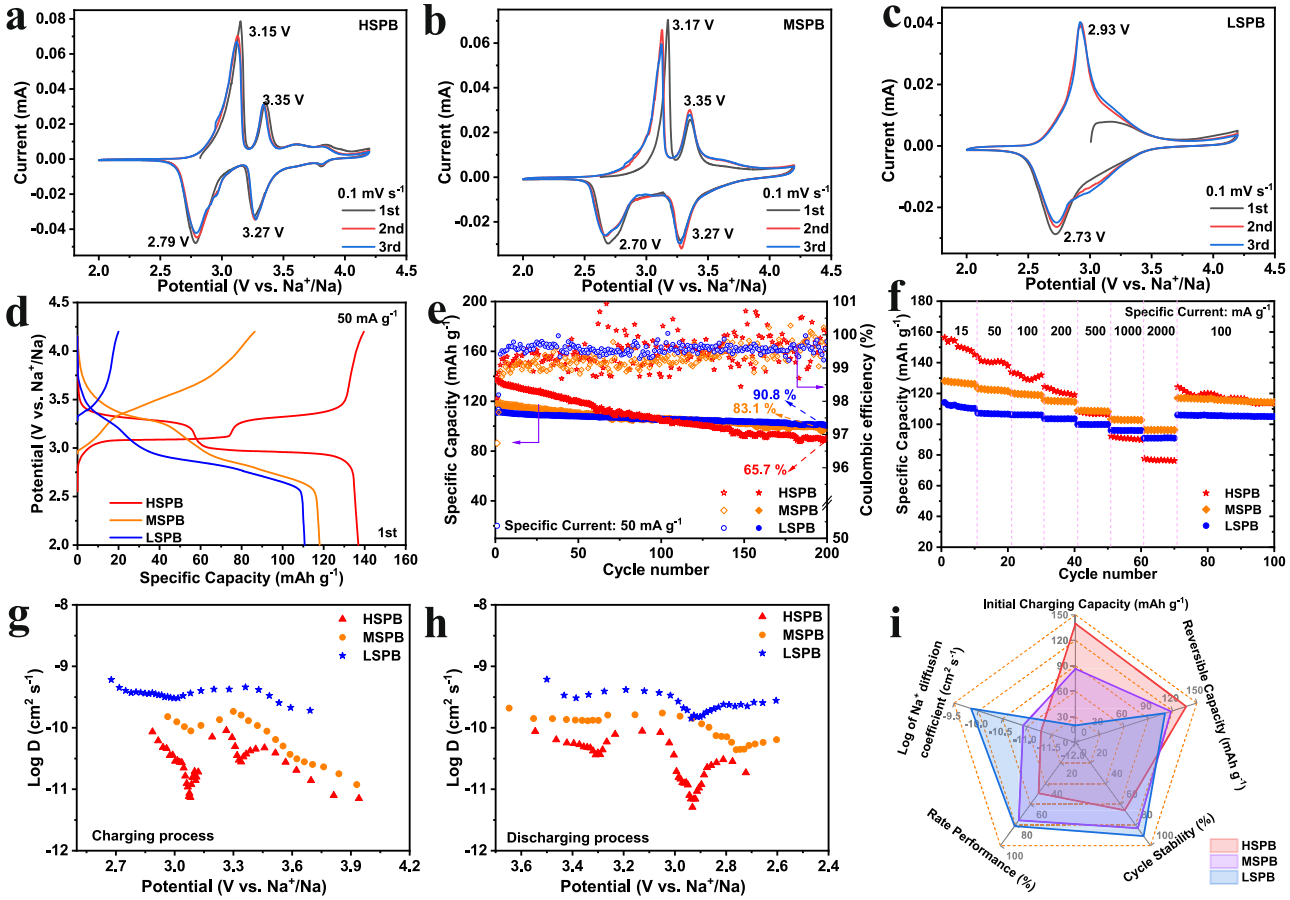

Fig. 2 | Electrochemical performance at 25 °C. a–**c** CV plots of HSPB, MSPB, and LSPB. **d** The 1st cycle galvanostatic charge/discharge plots of the three samples at 50 mA g^{-1}. Cycling performance (**e**) and (**f**) rate capacity of the three samples. The corresponding calculated D_{Na^+} of the three samples when charging (**g**) and discharging (**h**). **i** Radar chart for the trade-offs between log D_{Na^+}, rate performance, cycle stability, initial charging capacity, and reversible capacity among the three materials.

first as the samples were heated, then interstitial water located within the crystal framework, and finally, water that was chemically coordinated with the transition metal ions. As a result of the addition of a chelating agent, the adsorbed water in PBAs decreased significantly from 12.5% (LSPB) to 1.5% (HSPB). More water loss of HSPB occurred around 220 °C, implying more interstitial water in the framework. The reason for the increased amount of interstitial water in sodium-rich PBAs may be the slow nucleation rate, which means a long growth period and more water movement into the framework. A higher water content (adsorbed and interstitial) for sodium-free rather than sodium-rich PBA was found, which is consistent with the previous reports[16,18,38]. Consistent with the in-situ heating XRD data, LSPB underwent a rapid mass degradation after 275 °C, indicating the decomposition of the framework. HSPB maintained a relatively stable mass retention rate before 400 °C, however, which indicates a more stable skeleton and fewer defects.

Electrochemical investigations. According to the cyclic voltammetry (CV) plots (Fig. 2a, b), two strong and symmetrical redox pairs were observed around 3 V (high-spin Fe) and 3.3 V (low-spin Fe). Low-spin Fe is less redox active in LSPB, which may result from its many crystal defects and the high amounts of adsorbed water in its framework (Fig. 2c). During the discharge process, the low-spin Fe undergoes a reduction reaction from Fe^{3+} to Fe^{2+}. Once the low-spin Fe in HSPB has fully contributed its capacity, i.e., at around 60 mAh g^{-1}, the voltage drops almost vertically because of the completion of the reduction reaction as shown in Fig. 2d. High charging capacity (139.6 mAh g^{-1}) was achieved for the HSPB at 50 mA g^{-1} within the range of 2-4.2 V, benefitting from the high initial Na content (Fig. 2d). MSPB provided a capacity of 86.4 mAh g^{-1} in the 1st charging process while only 19.9 mAh g^{-1} was achieved for LSPB. Since LSPB does not contain potassium ions, the initial charging capacity may be mainly derived from the capacitance contribution of conductive carbon (Supplementary Fig. 8). After discharging, the reversible capacities of HSPB, MSPB, and LSPB were 136.9, 118.0, and 110.8 mAh g^{-1}, respectively. The low reversible capacity of LSPB is mainly due to structural deficiencies, including a high density of $Fe(CN)_6$ vacancies, which reduce active sites for sodium-ion insertion and extraction, limiting its capacity. A study of the cycling stability of the samples was performed at 50 mA g^{-1}, as shown in Fig. 2e and Supplementary Fig. 9. For capacity retention after 200 cycles, LSPB shows the highest retention level at 90.8%, while HSPB was only able to retain 65.7%. Although high initial reversible capacity was achieved by HSPB, the capacity fade after cycling makes it less promising for practical long-cycling-life SIBs. The reason for capacity decline needs to be further explored after analysis of HSPB and comparison with the results of MSPB and LSPB, which will be discussed in the next section. When the specific current was increased to 2000 mA g^{-1}, the LSPB provided a reversible capacity of 90.9 mAh g^{-1} (equal to 81.2% of its reversible capacity at 15 mA g^{-1} for LSPB), significantly better than for the HSPB (Fig. 2f). In addition, the galvanostatic intermittent titration technique (GITT) confirmed the fast reaction kinetics of LSPB during the charging/discharging process. The calculated sodium diffusion coefficient (D_{Na^+}) of LSPB was higher than that of HSPB, indicating a fast diffusion rate (Fig. 2g, h and

Supplementary Fig. 10). Considering practical applications, high specific energy, prolonged cycle life, and good rate capability are typically required for SIBs. An additional requirement for the cathode is to provide enough sodium ions to shuttle to an anode, such as hard carbon during charging. Therefore, radar plots were used to summarize the quality of the three PBAs exhibiting different electrochemical properties (Fig. 2i). Benefitting from its Na-rich structure, HSPB provided the most impressive initial charge capacity and reversible capacity, but it had poor rate performance and cycling. Despite having more water content and crystal defects, LSPB exhibited better cycling stability than Na-rich HSPB. This result shows that the capacity fading of common PBAs cannot be simply attributed to these two factors, and more attention should be paid to the morphology, active material loss, and lattice distortion after cycling.

Investigation of the capacity-fading mechanism. In order to gain a deeper understanding of the origins of the capacity fading of the HSPB, in-situ synchrotron XRD, SEM, and XPS were performed on the cycled electrodes, as well as density functional theory calculations (DFT). During the charging/discharging process, all the characteristic peaks are reversible, indicating that the crystal structure of the three PBAs can be maintained for the first two cycles (Fig. 3). As shown in Fig. 3a, d, rhombohedral iron-based PBAs (HSPB) experienced a phase transition process with large lattice distortion. In the first charge process, the (200), (220), and (400) planes are gradually shifted towards higher degrees, indicating some shrinkage of the unit cell. As a result of Na^+ extraction from the crystal framework, phase changes from rhombohedral to cubic were also observed in the HSPB electrode. Some published literatures regarded the small lattice change at high voltage as indicating a phase transition from the cubic phase to the tetragonal phase because of the little changes of c value[20,25]. This lattice change is relatively small (such as $a = b = 10.1926$ Å, $c = 10.2085$ Å), and it can also be considered as a Na^+-free cubic phase[24,25]. After the 1st discharging and 2nd discharging, the splitting phenomenon of the (220) peak was still obvious, as shown in Supplementary Fig. 11. Similar lattice changes (moving to higher/lower degree when charging/discharging) were also found in MSPB and LSPB, as shown in Fig. 3e, f. A change between sodium-rich and sodium-free states in the cubic phase was observed during cycling, which provides the entire reversible capacity through the redox reaction between Fe^{2+} and Fe^{3+}. Notably, LSPB exhibited an initially sodium-free cubic phase structure due to the absence of active sodium ions in the framework, as discussed above. The discharge operation was performed firstly during the in-situ XRD test, so the peak mainly shifted to the left first, followed by a shift to the right during charging, and it returned to its initial position after charging to 4.2 V. This changing trend and the main peak positions of LSPB are consistent with those of HSPB and MSPB, implying a changing process between sodium-rich and sodium-free states in the cubic phase. In addition, the cell volume change of HSPB at high voltage (where the peaks shifted a little to the left immediately after the peak positions were rightmost) is much larger than that of LSPB, which may also be an important reason for capacity fading. According to the in-situ XRD, the unit volume variations of the three samples were calculated in Fig. 3d–f. Notably, the rhombohedral structure of HSPB was subject to both shrinkage and expansion during the charging and discharging processes, with a large-volume distortion of 5.61%, which was greater than the distortion of MSPB and LSPB. During total charging and discharging processes, the unit volume can return to almost its initial value. The structure will become unstable, however, due to the gradually accumulating lattice strain from the lattice change. This phenomenon indicates that the structural variation of HSPB is greater than that of MSPB and LSPB, and it clarifies the lattice strain within two-phase transitions for rhombohedral HSPB (Fig. 3g).

In-situ XRD for the first two cycles indicated that HSPB showed a large lattice change due to more sodium ion shuttling, which is unfavorable for long-term cycling. In addition, the characterizations of the electrode sheet after long-term cycling can more specifically analyze the changes in the material during the cycling process. To further understand the rapid capacity fade of HSPB after long cycling, SEM observations were conducted on the electrodes of the three PBA cathodes after different cycles. As a model system, the pristine electrode sample and the electrodes after the 100^{th} and 200^{th} cycles were used to study the capacity fading mechanism because of the significant capacity decrease (~35%) in HSPB after 200 cycles. This capacity decay may be accompanied by significant structural, chemical, and morphological changes. As shown in the SEM images of the pristine electrodes (Fig. 4a, d), the HSPB preferred a quasi-cubic structure with a size of ~4 μm, while the LSPB featured irregular nanoparticles intertwined with conductive additives. The morphology of HSPB was broken after 100 cycles and almost collapsed after 200 cycles (Fig. 4b, c). This shows that fresh surfaces of HSPB will be exposed during the cycling process, which will sustainably consume the electrolyte and active Na^+ to form the cathode-electrolyte interphase. This may be a macroscopic manifestation brought about by lattice distortion during long-term cycling. In contrast, LSPB and MSPB maintained their morphology after cycling (Fig. 4e, f and Supplementary Fig. 12). It is also worth noting that many nanoparticles were formed on the surface of the HSPB after 100 cycles. These particles were clearly different from those of the conductive additives and more like particles bubbling from the inside (Supplementary Fig. 13). It can be seen from Supplementary Fig. 14 (secondary electron images on the left and corresponding backscattered electron images on the right) that the blue circled areas are the conductive additive, which are shown as dark areas in Supplementary Fig. 14b, d. There is no difference in brightness between the red-circled areas in the surface of HSPB, indicating that they do not show the conductive additive but surface nanoparticles produced by the material itself after cycling. Therefore, combining the image contrast of the backscattering mode and the SEM image analysis of the conductive additive in Supplementary Fig. 15, it can be speculated that the attached particles on the surface are the material itself. The reaction kinetics of HSPB electrodes after cycling were further studied by electrochemical impedance spectroscopy (EIS). The results of the EIS on HSPB (the pristine cell and the cell after 100/200 cycles) are shown in Fig. 4g, along with the equivalent circuit and impedance values that have been fitted. The medium-to-high-frequency range shows two partially overlapping semicircles due to the electrolyte-electrode interface film resistance (R2) and the charge-transfer resistance (R3). In the low-frequency range, the sloping line represents sodium diffusion (Warburg impedance, W1) and the bulk resistance of the cell (R1). The fitting value of R2 in the HSPB electrode changed from 172 Ω to 918 Ω after 100 cycles, which shows the increase in the resistance brought about by the electrolyte-electrode interphase film. On comparing the impedance after 200 cycles and 100 cycles, R3 changed greatly (from 1131 Ω to 3119 Ω) during this period, indicating that the charge-transfer resistance increased (Supplementary Table 4). Furthermore, the phase transition of HSPB was investigated again after multiple cycles. It can be seen from Fig. 4h that, after 100 cycles (discharged to 2 V), the splitting phenomenon of the (220) plane disappeared on the XRD pattern of HSPB, although it returns at the end of discharge state. The peak for the (200) planes of HSPB also shifted significantly after 100 cycles, indicating the reduction of Na ions in the structure. The in-situ synchrotron XRD of the HSPB after multiple cycles also confirmed that the double peak belonging to the (220) planes changed into a broad peak (Fig. 4i).

To understand the detailed reasons for the capacity decrease of HSPB, XPS was used to determine the chemical species formed on three PBA cathodes after different numbers of cycles (Fig. 5 and Supplementary Figs. 16–20). All the cycled electrodes were prepared and sealed in a glove box, followed by evacuating their containers and transferring them to the XPS instrument to avoid the influence on the

https://doi.org/10.1038/s41467-025-57663-3

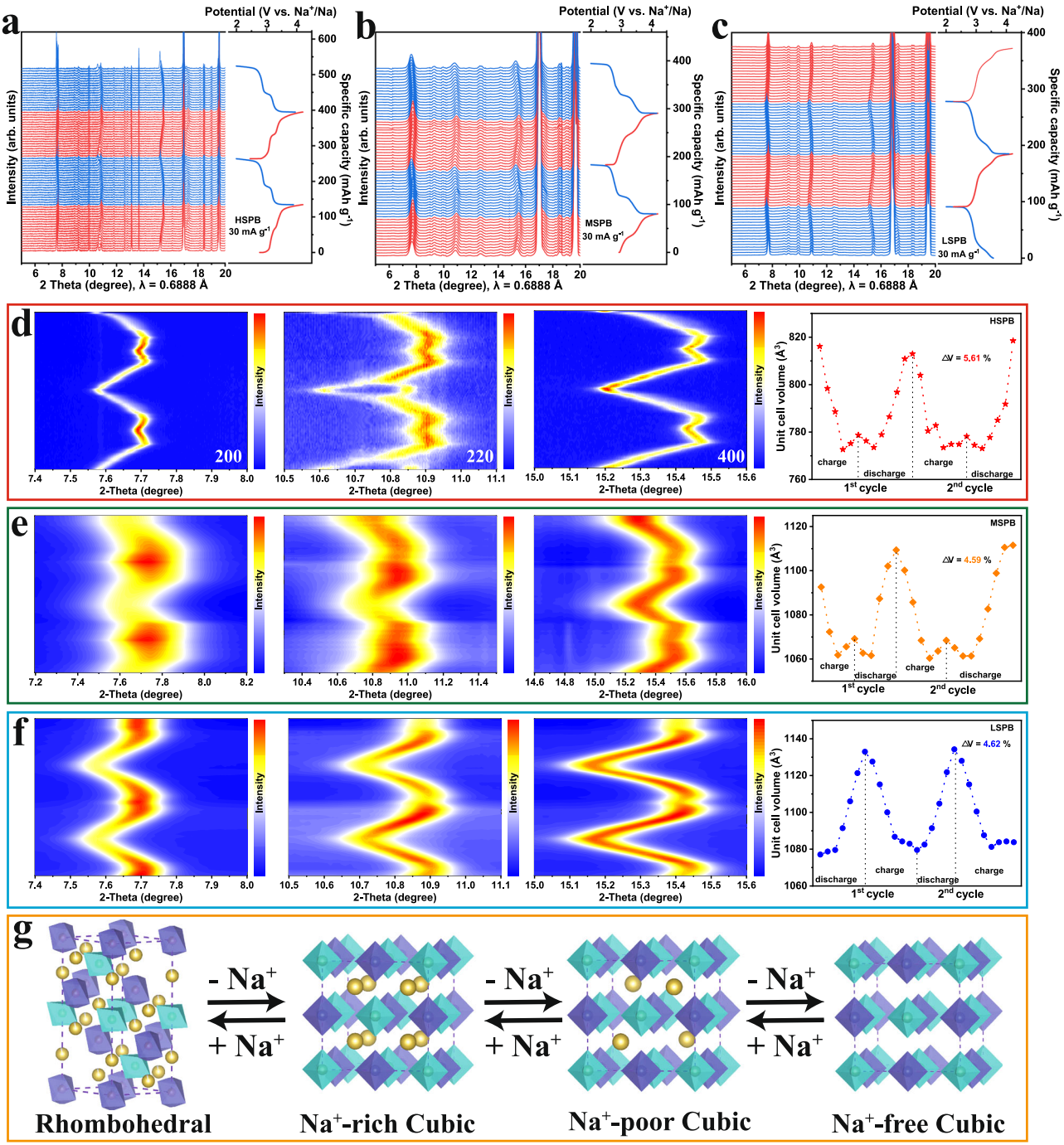

Fig. 3 | Investigations of phase transitions during cycling. a–**c** Synchrotron XRD spectra and galvanostatic charge/discharge plots of HSPB, MSPB, and LSPB. **d** Enlarged two-dimensional (2D) contour XRD images and volume variations for HSPB. **e** Enlarged 2D contour XRD images and volume variations for MSPB. **f** Enlarged 2D contour XRD images and volume variations for LSPB. **g** Schematic illustration of the phase transition mechanisms. The golden spheres represent sodium ions, and the purple and green octahedrons represent low-spin and high-spin iron.

electrodes of water and oxygen in the air. As shown in Fig. 5a, the Fe 2*p* spectra of pristine HSPB electrode exhibit two pairs of peaks located at 721.6/708.7 eV (Fe^{2+}) and 723.7/710.2 eV (Fe^{3+})[39–41]. The Fe^{3+}/Fe^{2+} ratio was increased after 100 cycles (reduced state), however, as shown in Fig. 5b. This means that some redox-active ferrous ions in the HSPB framework became inert Fe^{3+} sites and could not participate in subsequent cycles, causing a gradual decline in capacity. In addition, the peak at 530.6 eV in O 1*s* was assigned to Fe-O, which was generated by the dissolution of transition metal ions in the cell (Fig. 5c, d)[42,43]. The formation of Fe-O would result in a deterioration of the electrode and the irreversible loss of redox-active parts, which would further impair reversible capacity. Less Fe-O was generated in the MSPB/LSPB compared to the HSPB (Supplementary Fig. 17-18), indicating that inhibiting the dissolution of transition metal ions can improve cycling stability. Additionally, XPS depth analysis was performed to study the inactivation of redox centers. The intensity of the peak ascribed to Fe^{2+} was almost unchanged in pristine HSPB when the sputtering depth was increased. This peak was obviously and rapidly increased in cycled HSPB with increasing sputtering depth, however, indicating that the redox-active sites on the surface were deactivated while the interior

https://doi.org/10.1038/s41467-025-57663-3

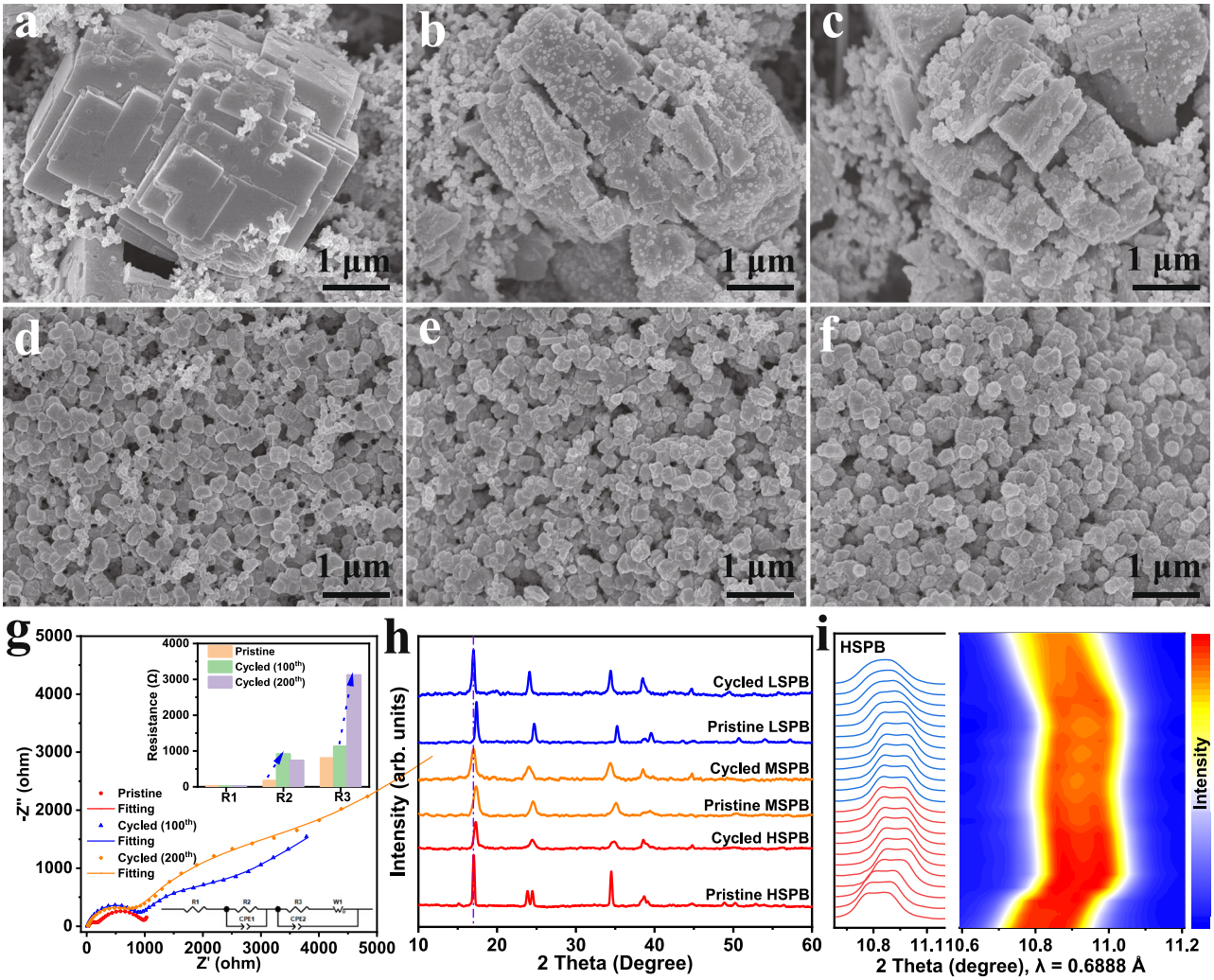

Fig. 4 | Capacity fading mechanism of HSPB electrode. Variations of morphology on the electrode: SEM images of pristine HSPB electrode (**a**), HSPB electrode after 100 cycles (**b**), and HSPB electrode after 200 cycles (**c**); SEM images of pristine LSPB electrode (**d**), LSPB electrode after 100 cycles (**e**), and LSPB electrode after 200 cycles (**f**). **g** Nyquist plots and the equivalent circuit modeling (inset, R1: the bulk resistance of the cell; R2: the electrolyte-electrode interface film resistance; R3: the charge-transfer resistance) of HSPB electrodes. **h** Laboratory-based XRD patterns of pristine electrodes and electrodes after 100 cycles. **i** Line spectra of in-situ synchrotron XRD and 2D contour image of HSPB after 50 cycles.

still maintained a high redox activity after multiple cycles (Fig. 5e, f). In addition, the cycled sodium metal and the separator (disassembled from the cell with HSPB as the cathode) were also tested, and the Fe 2*p* signals were found, further confirming the dissolution of transition metal in HSPB (Fig. 5g, h). The dissolution of iron ions is not caused by the formation of sodium dendrites or their contact with the cathode. Additionally, no voltage fluctuations indicative of short circuits were observed in the charging/discharging curves at different cycles. Instead, the dissolution is primarily attributed to structural and morphological changes in the cathode material during cycling.

To elucidate the time scale and mechanisms of Fe^{2+} deactivation, galvanostatic intermittent titration technique (GITT) experiments were conducted at various cycle numbers (Supplementary Fig. 21). At the high discharge plateau (C-coordinated low-spin Fe), D_{Na^+} remained stable across all cycles, indicating high low-spin Fe stability. Conversely, at the low discharge plateau (N-coordinated high-spin Fe), D_{Na^+} gradually declined with increasing cycles, suggesting progressive high-spin Fe^{2+} into Fe^{3+}. GITT data confirm this change is gradual rather than sudden. To further analyze Fe^{2+} deactivation, dQ/dV analysis (Supplementary Fig. 22a, b) was performed. The redox peaks of low-spin Fe remained prominent after 200 cycles, with minimal peak intensity or position changes, corroborating its stability. In contrast, the high-spin Fe redox peaks showed significant attenuation, accompanied by a discharge voltage decrease at the low plateau, indicating increased resistance and slower ion kinetics. By separating the capacity contributions of low-spin and high-spin Fe, low-spin Fe retained 88% of its initial capacity, while high-spin Fe capacity declined to 49% after 200 cycles, with deactivation accelerating notably after 40 cycles (Supplementary Fig. 22c–f). To quantify the correlation between lattice distortion, volume changes, and capacity retention, XRD measurements were conducted at different cycling stages (Supplementary Fig. 23). The results reveal that lattice parameters undergo progressive changes, with notable volume expansion and crystal distortion. In the early cycles (20 and 40 cycles), significant structural alterations were observed, including increases in the *a*-axis and unit cell volume by 0.3% and a decrease in the *c*-axis by 0.3%. These changes correlate with rapid capacity loss, indicating that increased lattice distortion impairs the material's ability to reversibly accommodate sodium ions. As cycling continued, the lattice distortion worsened, particularly after 80 cycles, with the *a*-axis and unit cell volume increasing by 0.5% and 0.6%, and the *c*-axis decreasing by 0.4%. After 100 cycles, the material transitioned from a rhombohedral to a cubic phase. SEM imaging and analysis are also conducted to investigate the propagation of cracks and the uniformity of degradation across the electrode (Supplementary Fig. 24). The degradation is observed to

https://doi.org/10.1038/s41467-025-57663-3

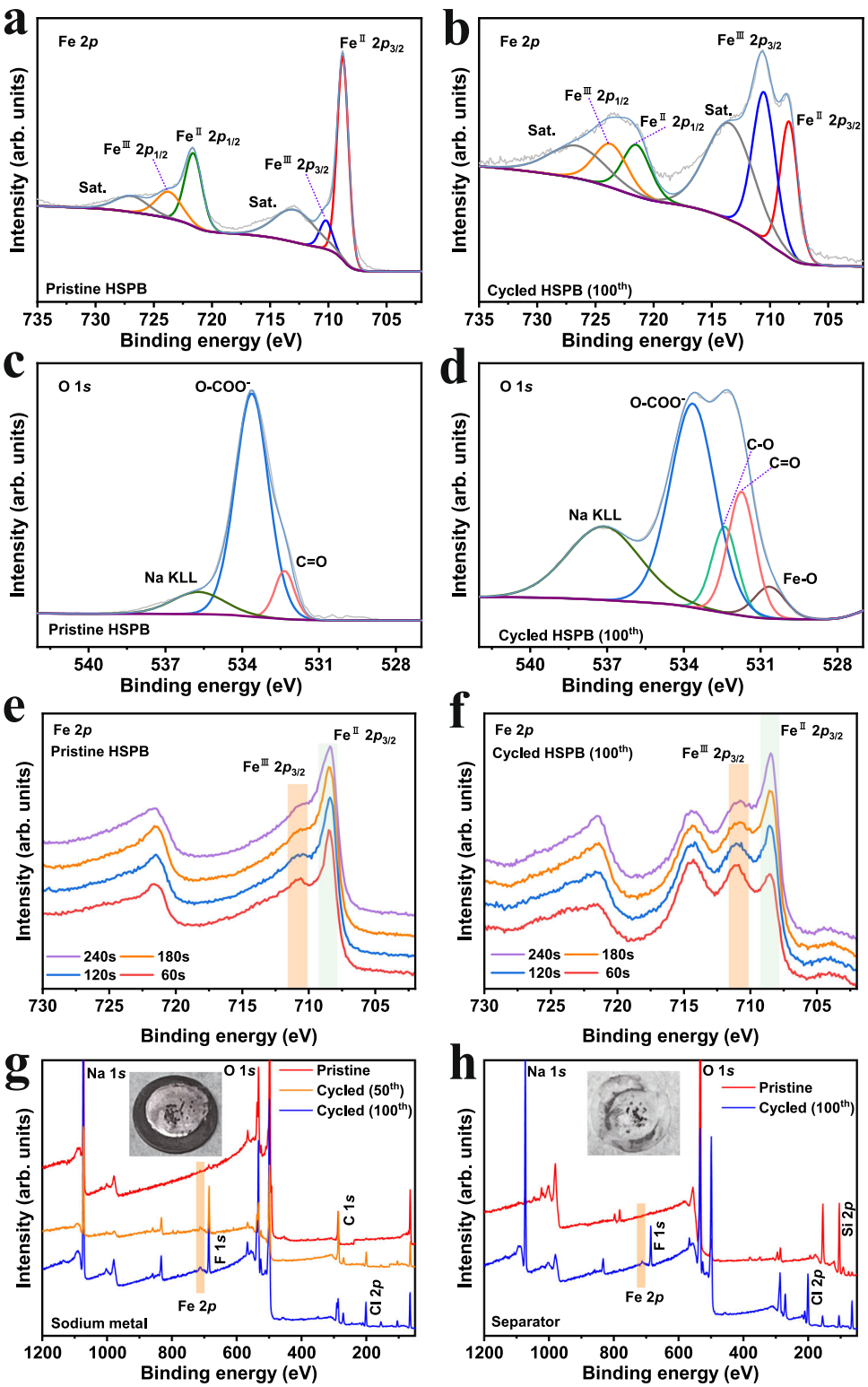

Fig. 5 | XPS survey on HSPB electrodes. Fe 2*p* spectra of pristine HSPB electrode (**a**) and HSPB electrode after 100 cycles (**b**). O 1*s* spectra of pristine HSPB electrode (**c**) and HSPB electrode after 100 cycles (**d**). Fe 2*p* depth profiles of pristine HSPB electrode (**e**) and HSPB electrode after 100 cycles (**f**) from different sputtering depths. XPS survey spectra of pristine sodium metal, sodium metal after 50 and 100 cycles (**g**) (with photographs shown in the insets) that were removed from the cycled cell using HSPB as cathode. XPS survey spectra of pristine separator, separator after 50 and 100 cycles (**h**) (with photographs shown in the insets) that were removed from the cycled cell using HSPB as cathode.

https://doi.org/10.1038/s41467-025-57663-3

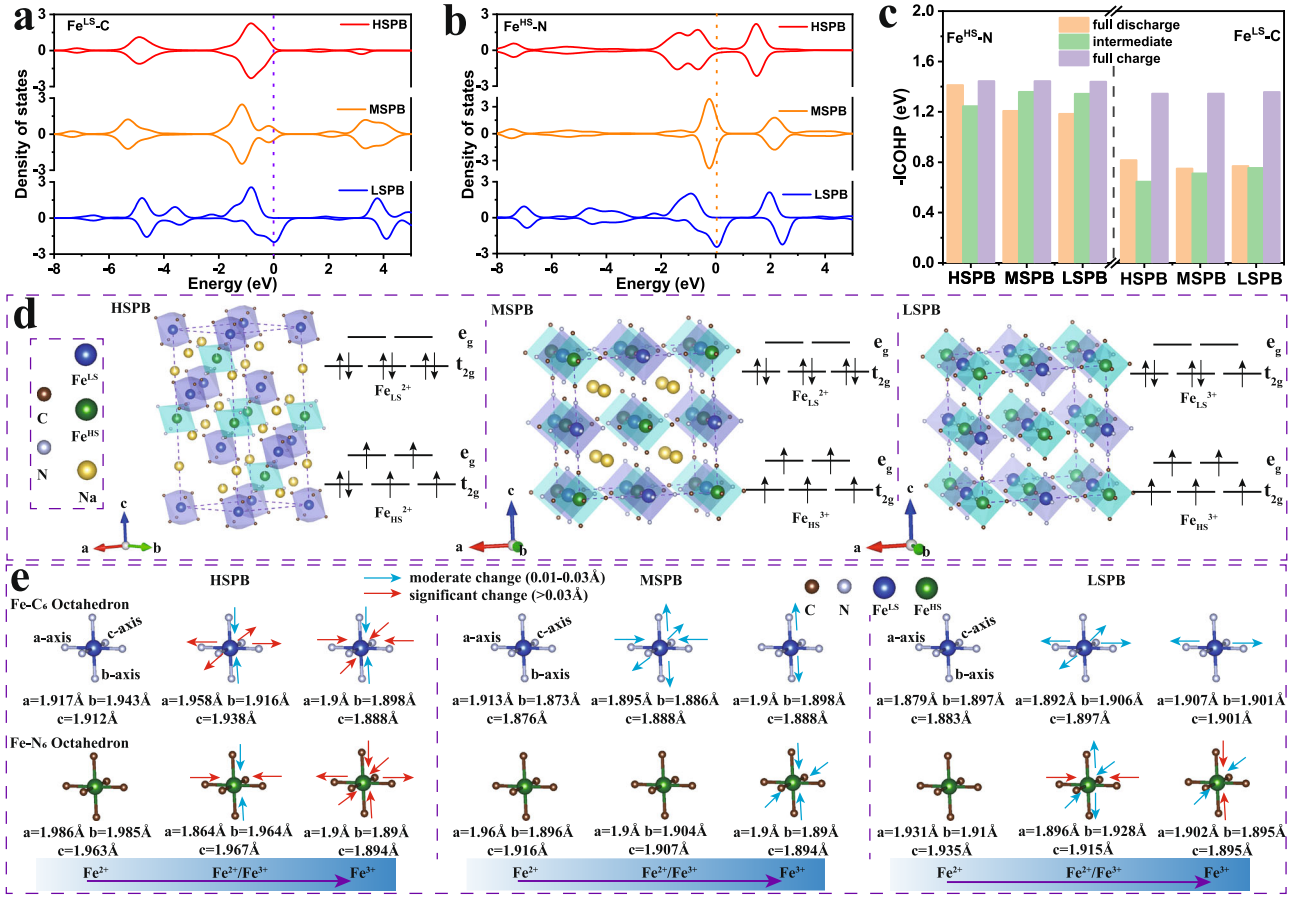

Fig. 6 | DFT calculations. a The pDOS of FeLS-*3d* states for the three samples. **b** The pDOS of FeHS-*3d* states for the three samples. **c** The -ICOHP values of FeHS-N (left) and FeLS-C (right). **d** Crystal structures showing the splitting of FeLS-*3d* and FeHS-*3d* states in the three PBAs. **e** DFT predictions of bond changes and the stretch directions in the charging process of HSPB, MSPB, and LSPB.

occur uniformly throughout the electrode rather than being localized to specific regions. In the early cycles, the material largely retains its original structure with only a few minor surface cracks. As the cycle number increases, the cracks become more numerous and larger, indicating the accumulation of structural stress. After 80 cycles, the cubic structure begins to break down, forming smaller particles, while cracks and fragmentation are widespread across the electrode after 200 cycles.

Afterward, density function theory (DFT) calculations were applied to examine the origins of capacity fading for the HSPB electrode. The coexistence of high-spin (HS) and low-spin (LS) states is well-established in PBAs. The intermediate spin (IS) states are generally unstable in PBAs. When the spin states of the divalent and trivalent iron ions are IS states, the electronic configurations are $(t_{2g})^5(e_g)^1$ and $(t_{2g})^4(e_g)^1$ respectively[44]. When e_g orbitals are unevenly occupied (neither fully filled nor half-filled), the system tends to reduce its total energy by distorting the coordination environment. This distortion breaks the orbital degeneracy, further splitting energy levels and lowering the energy. In addition, computational studies comparing the (LS, HS) and (LS, LS) configurations show that (LS, HS) is energetically more stable for Fe-based PBAs[45]. Figure 6a, b illustrates the projected density of states (pDOS) for high spin Fe-*3d* (FeHS-*3d*) and low spin Fe-*3d* (FeLS-*3d*). Compared to HSPB, the orbitals of FeHS-*3d* and FeLS-*3d* for LSPB and MSPB are close to the Fermi level, which implies their improved frame conductivity[46,47]. The above calculated result is consistent with the rate performance collected at three electrodes[45,48]. The integrated crystal orbital Hamiltonian population (ICOHP) values allow direct measurements of bond strengths[49]. During the whole charging process, the values of the Fe-N/Fe-C bonds of HSPB are lower than those of MSPB and LSPB in the intermediate state, implying a relatively weak bond strength of HSPB intermediates. Additionally, the -ICOHP value differences of Fe-N/Fe-C bonds for HSPB with various different states of charge are larger than that of LSPB/MSPB, which also has a negative influence on the structural stability. To confirm the lattice changes during cycling, DFT calculations were performed to determine the structural changes in the HSPB, MSPB, and LSPB during the Na-ion extraction process[50]. Figure 6d depicts the crystal structures of the three samples, where Fe atoms are coordinated with either six C or six N atoms (Fe-C and Fe-N octahedra, respectively). A further illustration of the corresponding electronic configurations and spin-charge densities of FeHS-*3d* and FeLS-*3d* can be found in Fig. 6d and Supplementary Fig. 25. The intercalation energy of HSPB is consistently lower than that of MSPB and LSPB, indicating stronger sodium-ion interactions in HSPB (Supplementary Fig. 26). While this enhances structural stability during sodium insertion, it leads to higher energy barriers during extraction, causing significant stress, microcracks, and lattice deformation over charging process. In contrast, the weaker sodium-ion interactions in MSPB and LSPB reduce structural stress during extraction, enabling smoother recovery and better structural stability over long-term cycling. As the lattice distortions are caused by the entire process of Na-ion movement in three samples, Fe-C and Fe-N octahedral sites were selected for the calculations. In general, huge distortion and moderate distortion were classified according to the change in the bond length. DFT studies show that Fe-C and Fe-N octahedra of HSPB have major distortions after the removal of Na^+,

https://doi.org/10.1038/s41467-025-57663-3

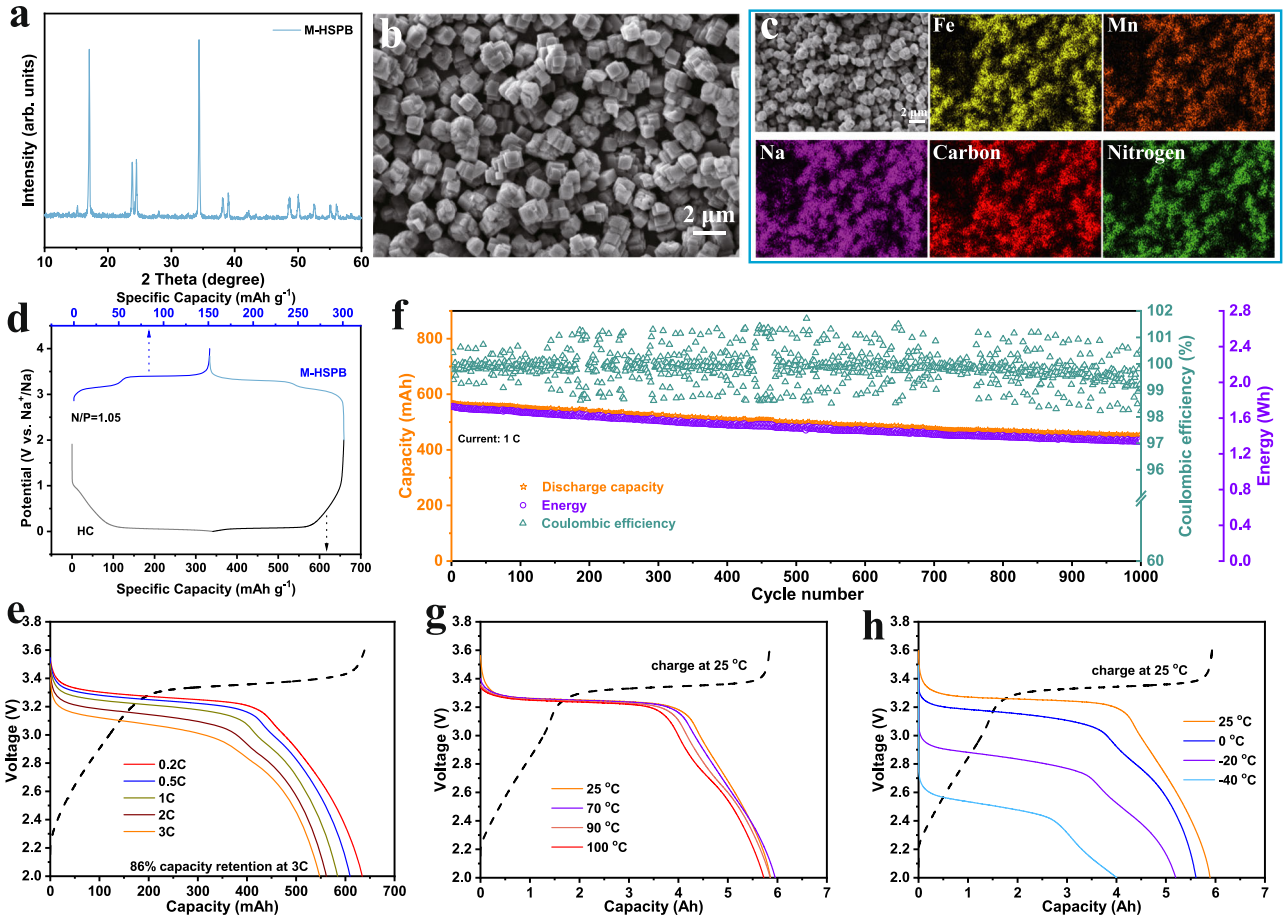

Fig. 7 | Modifications and practical cells. a XRD pattern of M-HSPB. SEM image of M-HSPB (**b**). **c** Element mapping and corresponding SEM image of M-HSPB. **d** The potential matchup shown by the charging/discharging profiles of M-HSPB and HC. **e** The rate performance of HC||M-HSPB 18650-type cell at room temperature. **f** Cycling performance of HC||M-HSPB 18650-type cell at room temperature. **g** The electrochemical performance of HC||M-HSPB 33140-type cell under high temperature (25 °C–100 °C). **h** The electrochemical performance of HC||M-HSPB 33140-type cell under low temperature (−40 °C–25 °C).

with almost all directions diminished (Fig. 6e). On the other hand, this also means that when sodium ions intercalate, Fe-C and Fe-N bonds in HSPB are violently stretched in all six directions. In contrast to HSPB, only two directions of Fe-N bonds are hugely shortened in LSPB, and four directions of Fe-C bonds remain almost uninfluenced during Na^+ extraction. Based on these results, HSPB undergoes a significant distortion during cycling, resulting in structural degradation and decreased capacity.

Dual-pronged strategy and practical cells investigation. From the results of the characterization and theoretical calculations of PBAs during cycling, it is evident that the primary degradation mechanism is due to significant lattice distortion during charge-discharge processes and subsequent irreversible phase transformation. These factors lead to the disintegration of the microscopic structure and the loss of active sites, particularly the deactivation of high-spin divalent iron ions. Therefore, a small amount of manganese ions was introduced into the high-spin sites to adjust the local coordination environment of high-spin Fe^{2+}. By regulating the solution environment, the nucleation of PBAs crystals was controlled, and a modified sodium-rich Prussian blue analogs (M-HSPB) were successfully synthesized. The XRD results for M-HSPB are shown in Fig. 7a, showing good crystallinity. After the introduction of some transition metal ions (Mn^{2+}) to modulate the coordination environment, the material retained rhombohedral phase without any change. By regulating the solution environment during synthesis, the M-HSPB crystals did not grow to approximately 4 μm like HSPB but exhibited a particle size distribution around 1 μm. Characterizations of LSPB indicate that smaller crystal nucleation helps maintain the integrity of the microstructure, reducing the surface crack during cycling. Elemental analysis confirms the uniform incorporation of Mn ions into the M-HSPB structure. The initial water content of the M-HSPB was determined through TGA, with a lower water content (Supplementary Fig. 27). A lower initial water content indicates fewer structural defects in M-HSPB, which helps maintain a stable framework during cycling. The in-situ synchrotron XRD was performed on the M-HSPB electrodes (Supplementary Fig. 28). Notably, during the charging and discharging processes, the volume distortion of M-HSPB is 4.45%, smaller than the distortion of HSPB. Smaller volume changes have a big benefit for long-cycle stability. These findings suggest that M-HSPB shows the ability to minimize stress during phase transitions. In addition, the introduction of Mn^{2+} into the HSPB structure significantly alters the electronic environment of Fe. Mn^{2+} doping at Fe-N sites modifies the charge distribution of the remaining Fe atoms, increasing the positive charge at Fe-N coordination sites (Supplementary Fig. 29). This change enhances the tendency of Fe to lose electrons, improving its redox activity. Additionally, the altered charge distribution boosts electronic conductivity, collectively explaining the enhanced cycling stability and redox performance of M-HSPB. With the dual regulation of coordination environment and nucleation, the prepared M-HSPB was employed in practical sodium-ion cylindrical batteries. As shown in Fig. 7d, the prepared M-HSPB was used as the cathode, while commercially available hard carbon (HC) served as the anode. After

balancing the capacities, HC||M-HSPB 18650/33140 type sodium-ion cylindrical batteries were assembled. As shown in Fig. 7e and Supplementary Fig. 30, the assembled HC||M-HSPB 18650-type cells exhibited good rate capability, retaining 86% of its capacity at 3 C. Moreover, due to the modulation of the local coordination environment and control of crystal nucleation, the prepared HC||M-HSPB exhibited stable cycling performance (Supplementary Fig. 31). After 1000 cycles, the capacity retention reached 80.1%, showing significantly improved stability compared to HSPB (Fig. 7f). Additionally, the voltage of cells remained stable during cycling, resulting in an energy retention rate of 77.6% after 1000 cycles. The 18650 batteries using HC||M-HSPB display good cycle stability than other full-cells with different reported PBA-based materials (Supplementary Table R5). Due to the lower internal resistance and wider market potential of larger cylindrical batteries, the performance of HC||M-HSPB in 33140 cylindrical batteries (Supplementary Fig. 32) was also investigated. Supplementary Fig. 33 presents the computed tomography picture of 33140 cylindrical battery, which adopts a full-tab design, clearly showing the cathode, anode, and separator. With the use of a high-temperature resistant separator, the 33140-type cells were able to operate normally at 100 °C. As shown in Fig. 7g, the discharge capacity retention at high temperatures was over 97%. In a low-temperature environment, 88% capacity retention was achieved at −20 °C compared to performance at 25 °C, and 68% capacity retention was maintained even at −40 °C (Fig. 7h). This demonstrates the potential of PBAs for applications of practical SIBs with a wide temperature range. The cylindrical cells were mainly designed to validate the practicality of the materials rather than to achieve high specific energy. The 18,650 cell (~26.5 g) achieved a specific energy of 68 Wh kg^{-1}, while the 33,140 cell (~174 g) reached 108 Wh kg^{-1}. While the theoretical specific energy of PBAs-based sodium-ion batteries can exceed 160 Wh kg^{-1} with advanced engineering, currently available commercial batteries of this type typically deliver 100–120 Wh kg^{-1}. These are primarily used in power-focused and wide-temperature applications rather than for maximizing specific energy, demonstrating their competitiveness in niche markets.

Discussion

In summary, by comparing three PBA materials with different crystal structures, defects, and water contents, the reasons for the capacity fading of PBAs were revealed using multiple characterization techniques at the macroscopic and microscopic levels. Although the HSPB with its Na-rich structure, has a high initial reversible capacity, the capacity continues to fade due to structural fragmentation caused by large distortions in subsequent cycles. In addition, the failure of active redox reactions on the electrode surface and the accumulated dissolution of transition metal ions during cycling are also important reasons for the capacity fading. This decay process is not affected by crystal defects or the high crystal water content of PBAs but is closely related to irreversible crystal/structural changes. Although some existing synthetic methods could reduce crystal defects and crystal water content by slowing the nucleation rate, these methods cannot prevent the structural distortion during cycling. Thus, a dual regulation strategy focused on the coordination environment and crystal nucleation growth is applied for PBAs. Benefiting from the regulation of the coordination environment by Mn^{2+} and the limitation of crystal growth size, the M-HSPB exhibits good crystallinity and cycle stability. As a practical demonstration, the designed 18650/33140 cylindrical cells using M-HSPB and hard carbon display enhanced cycling stability (80% capacity/energy retention after 1000 cycles) and wide temperature working ability (−40 °C–100 °C). Our work demonstrates the urgent need to re-examine the effects of changes in the crystal structure of PBA materials during cycling, such as lattice strain, irreversible phase transitions, volume changes, and structural degradation, and to understand how they affect capacity decrease. Future efforts should focus on developing efficient methods to improve the structure stability during cycling. Furthermore, tailoring PBA materials for specific applications, such as fast discharge or low-temperature environments, will expand their utility and accelerate industrial adoption. We believe that this study helps towards resolving the existing controversy over capacity degradation origin in PBAs and demonstrates their potential for practical SIBs with long cycle life and wide temperature range.

Methods

Preparation of materials

Chemicals were bought from Aladdin and used as received. Hard carbon (HC) was obtained from Wenzhou NaTech New Energy Technology Co., Ltd., and used directly as anode. Using a precipitation method, Fe-based Prussian Blue Analogues (PBAs) were prepared. In a typical synthesis of HSPB, solution A was prepared by mixing 6 mmol $FeSO_4{\bullet}7H_2O$ with 30 mmol sodium citrate in 80 mL deionized water. Solution B contained 6 mmol $Na_4Fe(CN)_6{\bullet}10H_2O$ dissolved in 80 mL of deionized water. After stirring for three hours under Ar protection, a pump (LongerPump Co., Ltd., BT100-2J) was used to slowly add solution A to solution B with 15 mL/h, and the mixed solution was stirred for a further three hours under Ar protection before being aged for 24 h. Three washes with deionized water and ethanol were performed, followed by 12 h of drying at 120 °C under vacuum. MSPB was prepared similarly except for solution A (3 mmol $Fe_2(SO_4)_3$ dissolved in 80 mL deionized water). LSPB samples were prepared as described above, except for solutions A (3 mmol $Fe_2(SO_4)_3$ dissolved in 80 mL deionized water) and B (6 mmol $K_3Fe(CN)_6$ dissolved in 80 mL deionized water). M-HSPB was prepared similarly like HSPB except for solution A (4 mmol $FeSO_4{\bullet}7H_2O$, 2 mmol $MnSO_4{\bullet}H_2O$, 3 mmol ascorbic acid, and 12 mmol sodium citrate dissolved in 80 mL deionized water).

Preparation of electrodes and electrochemical measurements

An electrode slurry for 2032-type coin cell was prepared by mixing the active materials (PBA samples), Super P, and poly(vinylidene fluoride) in a weight ratio of 7:2:1 with N-methyl pyrrolidone (Aladdin, 99.9%). The electrode was pasted on aluminum foil (15 μm, 99.6%, Hubei Fengsheng Electronic Technology Co., Ltd) and dried overnight in a vacuum at 100 °C. The PBA samples were compressed under 15 MPa and cut into disks (12 mm in diameter) with an areal mass density of ~2 mg cm^{-2} (~30 μm in thickness). For the assembly of 2032-type coin cells (containing positive and negative stainless steel shells, a piece of single-coated cathode electrode, sodium foil, separator, electrolyte, one round stainless steel (15 mm × 0.15 mm), and one stainless steel spring), a glove box filled with Ar with less than 0.01 ppm H_2O and O_2 was utilized. The anode and separator were respectively made up of fresh sodium metal (Aladdin, 99.7%, ~0.5 mm in thickness, 14 mm in diameter) and glass fiber (Whatman, GF/D, 16 mm in diameter, 675 μm in thickness). The electrolyte consisted of 1 M $NaClO_4$ in ethylene carbonate and diethyl carbonate (v:v = 1:1) containing 5 wt% fluoroethylene carbonate (Duoduo Chemical Technology Co., Ltd). The calculations of specific capacity and specific current are based on the active cathode material content (the cathode needs to be heated at 120 °C for 2 hours in the glove box to remove crystal water). The electrochemical measurements were conducted on a Neware battery cycler (CT-4008-5V10mA-164, Shenzhen, China) between 2.0 and 4.2 V at 25 °C ± 2 °C with constant current techniques. A CHI760D electrochemical workstation (Chenhua) was utilized for the cyclic voltammetry (CV, 0.1 mV s^{-1}, 2–4.2 V) and EIS measurements (5 mV amplitude, 10^{-2} Hz to 10^6 Hz, open-circuit potential). The Zview software was used to fit the EIS data. Galvanostatic intermittent titration technique (GITT) profiles were obtained from charge/discharge time for 15 min and interruption time for 60 min. For

each electrochemical experiment, at least three cells were tested. The data presented in the manuscript are from a single selected cell, a representative cell demonstrating median performance characteristics. For in situ XRD measurements, the cell components, including electrodes, electrolytes, and separator, were fabricated following the standard 2032-type coin cell excepting punching holes (5 mm in diameter) on the positive and negative stainless steel shells. These apertures were sealed using aluminum foil tape as window to ensure structural integrity during testing. For ex situ tests, the coin cells were disassembled in an Ar-filled glove box with water and oxygen content less than 0.01 ppm. The extracted electrodes were thoroughly washed with dimethyl carbonate (Aladdin, 99.9%) and dried at 100 °C to remove solvents in the glove box. For the assembly of cylindrical batteries, the cathode electrode slurry was prepared by mixing the active material (M-HSPB), Super P, and poly(vinylidene fluoride) in a weight ratio of 90:5:5 using N-methyl pyrrolidone as the solvent. The hard carbon (HC) anode electrodes were prepared using the same procedure, except the slurry was formulated with 93 wt% HC, 2 wt% Super P, and 5 wt% sodium alginates (SA) in water. The loading of positive electrode contained was 15–18 mg cm^{-2}, whereas that of the HC anode was 6–7 mg cm^{-2}. The negative-to-positive (N/P) ratio was maintained between 1.05 and 1.1 to ensure balanced capacity and optimal performance. All electrodes were through a calendering process (cathode: 1.4 g cm^{-3}, anode: 0.92 g cm^{-3}). The charge/discharge tests for cylindrical batteries were conducted over the voltage range of 2–3.6 V.

Materials and electrode characterization

Powder X-ray diffraction (XRD, Panalytical) was used to analyze the crystal structures of the as-synthesized samples. A calcination program from 20 °C to 400 °C at a heating rate of 5 °C min^{-1} under an argon (Ar) atmosphere was applied on the in-situ heating XRD. A field emission scanning electron microscope (JEOL, KSM-7500FA) equipped with an energy-dispersive X-ray spectrometer (EDS) was used to examine the morphology of the PBA samples. Raman spectroscopy was performed using a LabRAM HR800 (Horiba Jobin Yvon) spectrometer with a wavelength of 532 nm. The samples were analyzed using Fourier transform infrared spectroscopy (FTIR, Thermo Nicolet 670 FTIR spectrometer). Under an Ar atmosphere and with a heating rate of 5 °C, the thermogravimetry tests were conducted on a Netzsch STA 449F5 analyzer. X-ray photoelectron spectroscopy (XPS) data were collected using a Thermo Scientific Nexsa X-ray photoelectron spectrometer system. A sample holder with an inert atmosphere is used to transport the samples when testing XPS. XPS binding energies were calibrated using the C 1*s* peak (284.8 eV). X-ray absorption (XAS) studies were conducted at the XAS beamline of the Australian Synchrotron. In-situ XRD measurements (wavelength = 0.6888 Å) were performed at the Powder Diffraction beamline at the Australian Synchrotron using coin cells for tests. X-ray computed tomography was conducted to observe the inner structure changes by 3D reconstruction (Tianjin Sanying Precision Instruments Co., Ltd).

Density functional theory (DFT) calculations

The Dmol3 module was used to calculate the spin polarization with density functional theory. The Perdew-Burke-Ernzerhof functional approximation based on the generalized gradient approximation was used to describe the exchange-related energy. The Grimme dispersion-correction method was employed during both the structural optimization and the Density of States (DOS) calculations. The model of Prussian blue Analogs was constructed using 2 × 2 × 2 supercells surrounded by periodic boundary conditions. The core treatment utilized DFT Semi-core Pseudopots to reduce computational costs, and the DNP basis set was selected. To obtain plausible results, the energy and force convergence criteria in the structural optimization were 10^{-5} Ha and 0.02 Ha/Å, respectively, and the gamma-centered Monkhorst-Pack k-point grid was set to 3 × 3 × 3.

Data availability

Source data are provided with this paper. Extra data are also available from the corresponding author upon request. Source data are provided with this paper.

References

1. Zhao, Y. et al. Recycling of sodium-ion batteries. *Nat. Rev. Mater.* **8**, 623–634 (2023).
2. Liu, Y. et al. Advanced characterizations and measurements for sodium-ion batteries with NASICON-type cathode. *Mater. eSci.* **2**, 10–31 (2022).
3. Shi, Q. et al. Niobium-doped layered cathode material for high-power and low-temperature sodium-ion batteries. *Nat. Commun.* **13**, 3205 (2022).
4. Chen, X. et al. Zinc-ion hybrid supercapacitors: design strategies, challenges, and perspectives. *Carbon Neutralization* **1**, 159–188 (2022).
5. Zhang, H. et al. Organic small molecules with electrochemical-active phenolic enolate groups for ready-to-charge organic sodium-ion batteries. *Small Methods* **6**, 2200455 (2022).
6. Zhang, Y. et al. Construction of AlF_3 layer to improve $Na_{3.12}Fe_{2.44}(P_2O_7)_2$ interfacial stability for high temperature stable cycling. *Chem. Eng. J.* **430**, 132708 (2022).
7. Guo, J.-Z. et al. Emerging characterization techniques for delving polyanion-type cathode materials of sodium-ion batteries. *Mater. Today* **66**, 221–244 (2023).
8. Wang, K. et al. Precipitate-stabilized surface enabling high-performance $Na_{0.67}Ni_{0.33-x}Mn_{0.67}Zn_xO_2$ for sodium-ion battery. *eScience* **2**, 529–536 (2022).
9. Liu, X. Y., Cao, Y. & Sun, J. Defect engineering in Prussian blue analogs for high-performance sodium-ion batteries. *Adv. Energy Mater.* **12**, 2202532 (2022).
10. Zhang, H. et al. Organic cathode materials for sodium-ion batteries: from fundamental research to potential commercial application. *Adv. Funct. Mater.* **32**, 2107718 (2021).
11. Wu, Z.-H., Yu, Y.-X. & Chibisov, A. N. Density functional theory investigation on fast storage of sodium and potassium in Ni_2TeO_6 as a novel promising cathode material. *Mater. Today Energy* **37**, 101414 (2023).
12. Wu, Z.-H. & Yu, Y.-X. Regulating the electrochemical performance of $A_2Ni_2TeO_6$ (A = Na, K) as a cathode of alkali metal ion battery by 3 d transition metal substitution from a theoretical perspective. *ACS Appl. Energy Mater.* **7**, 8715–8725 (2024).
13. Sun, R. M. et al. Regulation of low-spin Fe of Mn-iron hexacyanoferrate for boosted potassium ion storage performance. *J. Power Sources* **556**, 232406 (2023).
14. Liu, X. H. et al. Advanced characterization techniques paving the way for commercialization of low-cost Prussian blue analog cathodes. *Adv. Funct. Mater.* **32**, 2108616 (2022).
15. Zhang, H. et al. Low-cost zinc substitution of iron-based Prussian blue analogs as long lifespan cathode materials for fast charging sodium-ion batteries. *Adv. Funct. Mater.* **33**, 2210725 (2022).
16. Wang, W. et al. Effect of eliminating water in Prussian blue cathode for sodium-ion batteries. *Adv. Funct. Mater.* **32**, 2111727 (2022).
17. Xie, B. et al. Recent progress of Prussian blue analogues as cathode materials for nonaqueous sodium-ion batteries. *Coord. Chem. Rev.* **460**, 214478 (2022).
18. Xie, J. et al. Self-healing of Prussian blue analogues with electrochemically driven morphological rejuvenation. *Adv. Mater.* **34**, e2205625 (2022).
19. Zhang, H. et al. Long-cycle-life cathode materials for sodium-ion batteries toward large-scale energy storage systems. *Adv. Energy Mater.* **13**, 2300149 (2023).

20. Chen, Z. Y., Fu, X. Y., Zhang, L. L., Yan, B. & Yang, X. L. High-performance Fe-based prussian blue cathode material for enhancing the activity of low-spin Fe by Cu doping. *ACS Appl. Mater. Inter.* **14**, 5506–5513 (2022).
21. Zhang, H. et al. Prussian blue analogues with optimized crystal plane orientation and low crystal defects toward 450 Wh kg^{-1} alkali-ion. *Batteries. Angew. Chem. Int. Ed.* **62**, e202303953 (2023).
22. Ge, J., Fan, L., Rao, A. M., Zhou, J. & Lu, B. Surface-substituted Prussian blue analogue cathode for sustainable potassium-ion batteries. *Nat. Sustain.* **5**, 225–234 (2021).
23. Peng, J. et al. Ball milling solid-state synthesis of highly crystalline Prussian blue analogue $Na_{2-x}MnFe(CN)_6$ cathodes for all-climate sodium-ion batteries. *Angew. Chem. Int. Ed.* **61**, e202205867 (2022).
24. Wang, W. et al. Understanding rhombohedral iron hexacyanoferrate with three different sodium positions for high power and long stability sodium-ion battery. *Energy Storage Mater.* **30**, 42–51 (2020).
25. Wang, W. et al. Reversible structural evolution of sodium-rich rhombohedral Prussian blue for sodium-ion batteries. *Nat. Commun.* **11**, 980 (2020).
26. Liu, T. et al. Origin of structural degradation in Li-rich layered oxide cathode. *Nature* **606**, 305–312 (2022).
27. Liu, X. H. et al. A NASICON-typed $Na_4Mn_{0.5}Fe_{0.5}Al(PO_4)_3$ cathode for low-cost and high-energy sodium-ion batteries. *Carbon Neutralization* **1**, 49–58 (2022).
28. Xu, G. L. et al. Native lattice strain induced structural earthquake in sodium layered oxide cathodes. *Nat. Commun.* **13**, 436 (2022).
29. Liu, S. et al. Regulating Na occupation in P2-type layered oxide cathode for all-climate sodium-ion batteries. *Adv. Energy Mater.* **13**, 2203521 (2023).
30. Fu, F. et al. Entropy and crystal-facet modulation of P2-type layered cathodes for long-lasting sodium-based batteries. *Nat. Commun.* **13**, 2826 (2022).
31. Cheng, Z. et al. A rational biphasic tailoring strategy enabling high-performance layered cathodes for sodium-ion. *Batteries. Angew. Chem. Int. Ed.* **61**, e202117728 (2022).
32. Gao, Y. et al. Low-cost polyanion-type sulfate cathode for sodium-ion battery. *Adv. Energy Mater.* **11**, 2101751 (2021).
33. Ma, Y. et al. High-entropy metal-organic frameworks for highly reversible sodium storage. *Adv. Mater.* **33**, 2101342 (2021).
34. Luo, P. et al. Incorporating near-pseudocapacitance insertion Ni/Co-based hexacyanoferrate and low-cost metallic Zn for aqueous K-ion batteries. *ChemSusChem* **15**, e202200706 (2022).
35. Larson, A. C. & Dreele, R. B. V. General structure analysis system (GSAS) (Report LAUR 86-748, Los Alamos National Laboratory, 2004).
36. Zhao, Z. et al. Switching optimally balanced Fe–N interaction enables extremely stable energy storage. *Energy Environ. Mater.* **6**, e12342 (2022).
37. Gao, C. et al. Coexistence of two coordinated states contributing to high-voltage and long-life Prussian blue cathode for potassium ion battery. *Chem. Eng. J.* **431**, 133926 (2022).
38. Shi, L. et al. Co-precipitation synthesis control for sodium ion adsorption capacity and cycle life of copper hexacyanoferrate electrodes in battery electrode deionization. *Chem. Eng. J.* **435**, 135001 (2022).
39. Aulia, S. et al. Oxygen plasma-activated NiFe Prussian blue analogues interconnected N-doped carbon nanotubes as a bifunctional electrocatalyst for a rechargeable zinc–air battery. *ACS Appl. Energ. Mater.* **5**, 9801–9810 (2022).
40. Xie, B. et al. Interface reinforcement of a Prussian blue cathode using a non-flammable Co-solvent cresyl diphenyl phosphate for a high-safety Na-ion battery. *ACS Sustain. Chem. Eng.* **9**, 5809–5817 (2021).
41. Jiang, M. et al. Balanced coordination enables low-defect Prussian blue for superfast and ultrastable sodium energy storage. *Nano Energy* **102**, 107708 (2022).
42. Li, X. et al. Topotactic epitaxy self-assembly of potassium manganese hexacyanoferrate superstructures for highly reversible sodium-ion batteries. *ACS Nano* **16**, 453–461 (2022).
43. Xie, B. et al. An interface-reinforced rhombohedral Prussian blue analogue in semi-solid state electrolyte for sodium-ion battery. *Energy Storage Mater.* **36**, 99–107 (2021).
44. Nishino, M., Kubo, S., Yoshioka, Y., Nakamura, A. & Yamaguchi, K. Theoretical studies on magnetic interactions in Prussian blue analogs and active controls of spin states by external fields. *Mol. Cryst. Liq. Cryst.* **305**, 109–128 (1997).
45. Hurlbutt, K., Giustino, F., Pasta, M. & Volonakis, G. Electronic structure and electron-transport properties of three metal hexacyanoferrates. *Chem. Mater.* **33**, 7067–7074 (2021).
46. Xu, Z. et al. High-performance Ni/Fe-codoped manganese hexacyanoferrate by scale-up synthesis for practical Na-ion batteries. *Mater. Today Sustain.* **18**, 100113 (2022).
47. Zhang, L. L. et al. Ternary Ni-based Prussian blue analogue with superior sodium storage performance induced by synergistic effect of Co and Fe. *Carbon Energy* **3**, 827–839 (2021).
48. Wang, Y. P., Hou, B. P., Cao, X. R., Wu, S. Q. & Zhu, Z. Z. Structural evolution, redox mechanism, and ionic diffusion in rhombohedral $Na_2FeFe(CN)_6$ for sodium-ion batteries: first-principles calculations. *J. Electrochem. Soc.* **169**, 010525 (2022).
49. Keshri, S. P. & Pati, S. K. d-orbital-driven low lattice thermal conductivity in TiRhBi: a root for potential thermoelectric and microelectronic performance. *ACS Appl. Energy Mater.* **5**, 13590–13599 (2022).
50. Wang, Z. et al. Regulation of ferric iron vacancy for Prussian blue analogue cathode to realize high-performance potassium ion storage. *Nano Energy* **98**, 107243 (2022).

Acknowledgements

The authors acknowledge their financial support from the National Natural Science Foundation of China (Grant Numbers: 52250710680 [S.L.C.], 52171217 [S.L.C.], 22065017 [X.D.C.], 52402213 [Y.G.]), High-end Foreign Experts Recruitment Plan of China (G2023016009L [J.Z.W.]), Basic Research Project of WenZhou City (2024G0197 [H.Z.], 2024G0195 [Y.G.], G20240014[L.L]) and China Postdoctoral Science Foundation (Grant Numbers: 2023M740011 [Y.G.], GZC20230009 [Y.G.]), and the Jiangxi Provincial Natural Science Foundation (20224BAB214019 [X.D.C.], 20232BAB204024 [X.D.C.]). The authors are grateful to Dr. Bernt Johannessen at the Australian Nuclear Science and Technology Organization for collecting the XAS results. The authors are grateful for the support and equipment provided by the Electron Microscopy Centre at the University of Wollongong. The authors acknowledge the National Supercomputing Center in Shenzhen for providing computational resources and Materials Studio (version and module). The authors thank Dr. Tania Silver for thorough examination of the manuscript.

Author contributions

H.Z. and S.L.C. conceived the idea and designed the experiments together. H.Z., J.Y.L., Y.G., Y.M.F., H.X.L., and Q.F.G. performed characterizations and analysed the obtained data. H.Z. and Y.G. wrote the original manuscript. J.H.L., C.F.G., and X.D.C. conducted and analyzed the DFT calculations. X.H.L., X.Q.W., and Y.L. assembled and tested the 18650/33140-type cylinder cell. Y.G., X.D.C., L.L., J.Z.W., and S.L.C. gave advice to the research, revised the manuscript and supervised this work.

Competing interests

The authors declare no competing interests.

Additional information

Supplementary information The online version contains supplementary material available at https://doi.org/10.1038/s41467-025-57663-3.

Correspondence and requests for materials should be addressed to Yun Gao, Xiudong Chen, Li Li or Shu-Lei Chou.

Peer review information *Nature Communications* thanks Yang-Xin Yu and the other anonymous reviewer(s) for their contribution to the peer review of this work. A peer review file is available.